

Deployable System for Crash-Load Attenuation

Sotiris Kellas, PhD
Senior Lead Engineer
General Dynamics – AIS
NASA Langley Research Center, Hampton VA
s.kellas@larc.nasa.gov
sotiris.kellas@GD-AIS.com

Karen E. Jackson, PhD
Aerospace Engineer
Structural Dynamics Branch
NASA Langley Research Center, Hampton VA
karen.e.jackson-1@nasa.gov

Abstract

An externally deployable honeycomb structure is investigated with respect to crash energy management for light aircraft. The new concept utilizes an expandable honeycomb-like structure to absorb impact energy by crushing. Distinguished by flexible hinges between cell wall junctions that enable effortless deployment, the new energy absorber offers most of the desirable features of an external airbag system without the limitations of poor shear stability, system complexity, and timing sensitivity. Like conventional honeycomb, once expanded, the energy absorber is transformed into a crush efficient and stable cellular structure. Other advantages, afforded by the flexible hinge feature, include a variety of deployment options such as linear, radial, and/or hybrid deployment methods. Radial deployment is utilized when omnidirectional cushioning is required. Linear deployment offers better efficiency, which is preferred when the impact orientation is known in advance. Several energy absorbers utilizing different deployment modes could also be combined to optimize overall performance and/or improve system reliability as outlined in the paper. Results from a series of component and full scale demonstration tests are presented as well as typical deployment techniques and mechanisms. LS-DYNA analytical simulations of selected tests are also presented.

1. Introduction

Landing and crash energy management systems, which dissipate energy by stroking, can be grouped into two general categories. The first category consists of deployable devices such as hydraulic or pneumatic landing gears, vented airbags [1, 2], non-vented airbags [3, 4], and hybrid airbag systems [5]. Non deployable, or passive, energy absorbers belong to the second category which includes crushable honeycombs and cellular solids [6-9].

By and large, the type of crash energy management system chosen is governed by factors such as available volume, expected vehicle attitude and velocity at impact, mass allotment, and system reliability. Deployable systems offer unique advantages including efficient packaging and relatively large available stroke; however, due to their complexity, they are generally less reliable than passive systems.

External airbag systems have been utilized in many different aerospace applications. The most notable examples include the F-111 crew-escape module, which is described in Reference [1] (plug-vented air bags), and the Mars Pathfinder [3] (non-vented air bags). Typically, non-vented airbag systems have an inherent degree of springiness due to the residual gas pressure, which causes the vehicle to bounce several times before it comes to a complete rest. To offer adequate protection, the airbag is required to cover the entire vehicle, which generally leads to a heavier and more complex system. Because of sequential energy absorption (bouncing), non-vented airbag systems are not suitable for manned applications. Vented bags are generally more efficient energy dissipaters, when compared to non-vented systems. These can be grouped into two general categories: automobile type airbags [2], which rely on time sensitive deployment in order to operate correctly, and bags with blow-out plugs [1, 5] which vent when a predetermined pressure is sensed. Unfortunately, when used on aircraft to improve crashworthiness, serious reliability issues can offset potential advantages in energy absorption.

In the case of automobile-type airbags, which have been considered for external use on rotorcraft to mitigate crash loads [2], precise determination of impending impact over varying terrain is required which is a very challenging problem. For the plug-vented system (assuming that it can be inflated fast enough and all other sensors and systems function correctly) serious reliability issues can still arise when venting is partially or totally impaired due to the vehicle's unforeseen impact attitude. When gas is trapped, due to choked vents, these systems can cause vehicle

tumbling as was demonstrated clearly by the F-111 crew-escape module airbag system testing. Finally, all gas-filled airbag systems suffer from low shear stability, loading-rate sensitivity, impact/venting synchronization (especially when multiple airbags are used), and sensitivity to extreme landing surface features such as rocks and steep slopes. Consequently, extensive testing and/or analysis are often required for system development and qualification as was demonstrated by the F-111 program.

In order to avoid bottoming out, which is an inevitable negative aspect of vented airbags; a hybrid airbag approach was proposed [5]. The system consists of an internal non-vented bag (anti-bottoming) within a larger external vented bag (energy absorber). While this approach addresses the bottoming out issue, it does lead to a heavier and more complex system. Moreover, the non-vented bag is essentially a spring, which under certain attitude conditions could contribute to vehicle tumbling.

To address the airbag shear issue, Mehaffie [9] studied the foam filled airbag system for the recovery of small pilotless aircraft. While this concept appears to provide a viable solution to shear, time sensitive foam hardening and excess weight make it inappropriate for crashworthiness applications

2. Deployable Honeycomb – Concept Description

The deployable honeycomb Energy Absorber (EA) possesses most of the desirable features of a deployable airbag system while overcoming most of their limitations. As with the Bixby [7] and Schafer [8] concepts, the new energy absorber utilizes an expandable honeycomb-like structure to absorb impact energy by crushing. However, unlike any other cellular energy absorber in use today, the new concept utilizes a unique and patented flexible hinge at each junction of its cell walls. This feature enables almost any size and strength energy absorber to be fabricated and readily deployed either radially (omnidirectional energy absorption) or linearly (unidirectional energy absorption). Like conventional honeycomb, once expanded the new energy absorber is transformed into an efficient orthotropic cellular structure, with greater strength and stiffness along the cell axis as compared to the transverse directions. An example of an isolated cell-wall junction is shown in the schematic of Figure 1 and an actual photograph of a stitched junction in Figure 2.

Typically the hinge consists of a fabric made of relatively strong, stiff, and tough fibers such as spectra, aramid, vectran, or technora. Other flexible materials can also be used for the construction of the hinges; however, advanced fiber reinforced fabrics are thought to offer some unique opportunities for structural tailoring.

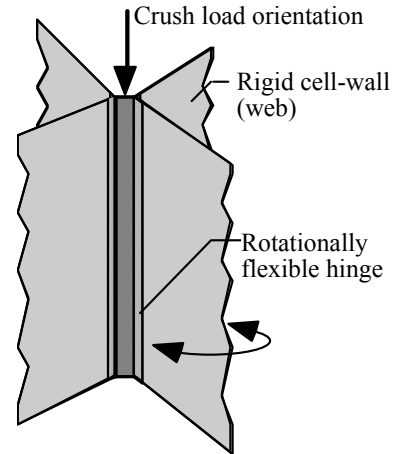


Fig. 1. Schematic of the junction (hinge) of a square cell deployable structure.

Examples of properties that can be optimized, individually or collectively, include minimal deployment force, shear rigidity, shear strength, hinge tearing resistance, and specific energy absorption.



Fig. 2. Photograph of square cell junction fabricated of Kevlar 129 and E-glass fabrics. A zigzag stitch pattern was used to eliminate delamination between the glass and the Kevlar plies. The hinge is made of Kevlar 129 with the fibers oriented at $\pm 45^\circ$ with respect to the hinge axis.

The flexible hinge enables various methods of expanding the cellular structure with the most basic ones shown in Figures 3-5. The linear expansion mode, which is depicted in the schematic of Figure 3, represents the simplest mode. When expanded in this fashion the energy absorber produces higher specific energy absorption due to a more efficient volumetric expansion (lower effective expanded density).

However, radial deployment (Figure 4) produces an energy absorber with better omnidirectional capability.

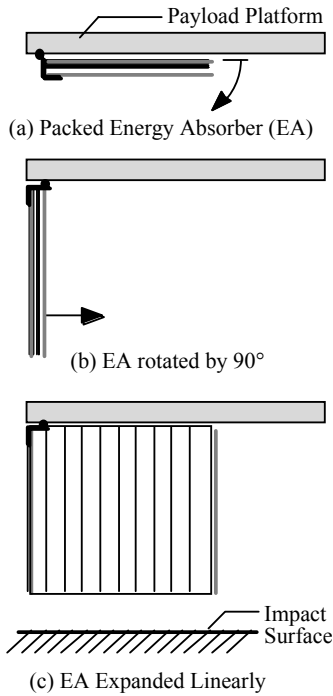


Fig. 3. Basic steps required for linear deployment of a packed energy absorber. Deployment mechanisms could include springs or actuators of various kinds.

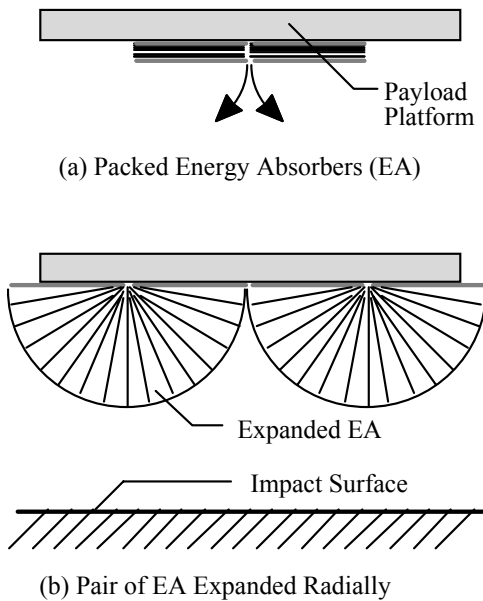
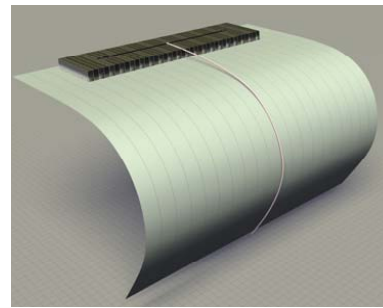


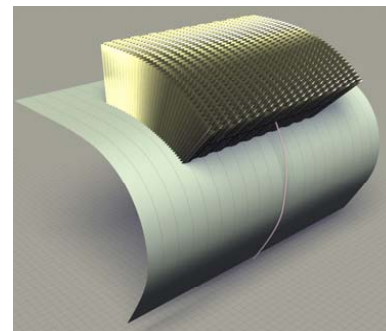
Fig. 4. Radial deployment of two energy absorbers. EA shape can be spherical, cylindrical, or any desired cross section. Note that deployment greater than 180° is possible if more vehicle coverage is required.

Because most practical applications involve curved rather than flat surfaces, the two basic deployment methods can be

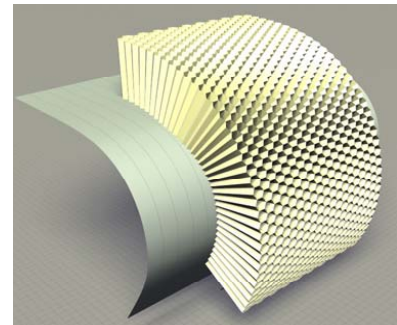
combined into a hybrid approach as shown in Figure 5. To minimize the expanded density of the energy absorber, the cells are tapered, as shown in Figure 5(c).



(a) EA packed



(b) EA partially deployed



(c) EA fully deployed

Fig. 5. Hybrid deployment example. Energy absorber is deployed over a curved surface.

An artist's conception of how the energy absorber could be used on a rotorcraft to improve its crashworthiness is shown in Figure 6. For this application the energy absorber would be stowed under a frangible (or removable) aerodynamic cowling until a command is given to deploy the energy absorbers.



Fig. 6. Artist's rendition of a rotorcraft with a set of energy absorbers deployed. The front energy absorbers are shaped to allow for egress. The flexible cover that would normally be used to cover the outer surface of the EA is not shown.

2.1 Energy Absorber Fabrication

Methods similar to the ones employed in the assembly of conventional aluminum honeycombs are also used in the fabrication of the deployable honeycomb. For conventional honeycombs, a series of parallel strips of adhesive are applied to flat sheets of ductile material using an automated process. Several sheets of material are then placed on top of each other such that the adhesive strips are staggered, as shown in Figure 7.

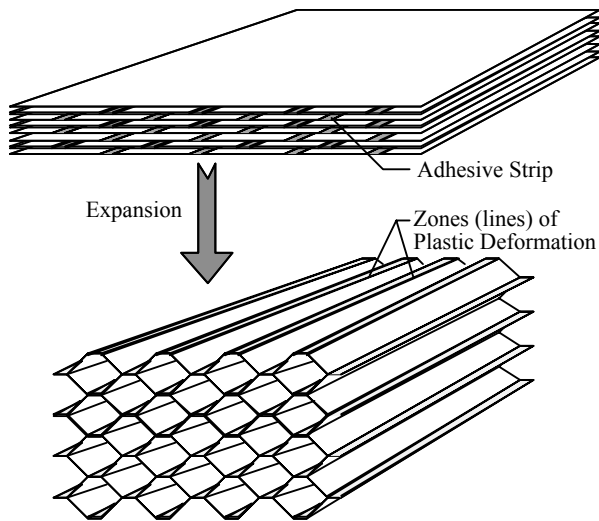


Fig. 7. Schematic of typical fabrication method used in the production of conventional honeycombs.

Following curing of the adhesive bonds, the flat assembly is expanded to a honeycomb-like cellular structure. With the exception of paper honeycombs and very thin aluminum foils, expansion is irreversible and a large amount of energy

is needed to complete the process, since the cell-wall material is required to deform plastically at every cell junction.

A similar process is used in the fabrication of the deployable energy absorber. The flat homogeneous sheets that form the cell-walls of the conventional honeycomb are replaced with sheets that contain hinge lines, as shown in Figure 8. Integration of several sheets of material is accomplished either by bonding (as with the panel in Figure 8), or by stitching (as with the stitched junction shown in Figure 2).



Fig. 8. Typical panel used in the fabrication of a deployable honeycomb structure showing the integrated hinge lines.

2.2 Deployment Systems

A variety of deployment mechanisms can be utilized depending on factors such as required deployment speed, EA system mass, cost and mode of deployment. It is thought that mechanical energy storage mechanisms, such as torsion springs and elastic hinges at the axis of rotation can offer the simplest and most cost effective deployment method. Using preloaded springs (one or two for radial and linear deployment, respectively) the energy absorber(s) can be packed and held in place under a cowling. Deployment can be enabled when the cowling is pyrotechnically separated from the vehicle.

In general, the deployment system consists of:

- (a) Sliding hinge (or multiple hinges) to help secure the energy absorber edge to the platform while enabling rotation of the packed energy absorber prior to expansion.
- (b) A latch or a release mechanism that would free the energy absorber from its stowed configuration.
- (c) Actuator(s) to lift the energy absorber and pull it open.
- (d) A series of tie downs to secure the energy absorber to the platform and ensure global stability. These could be rails, straps, or a combination of the two.

While the expanded energy absorber is inherently rigid in shear due to its cellular nature, global shear stability can be

enhanced further by the use of tie down straps as shown in Figure 9.

To date, several actuation methods have been demonstrated including mechanical, pneumatic, and mechanical/pneumatic combinations. In a typical mechanical actuation system the EA is pulled upright and opened by the stabilizing straps, and secured to the platform. A simple method is to apply tension by gathering the strap on an electric-motor driven spool.



Fig. 9. EA installed on a test article in preparation for a drop test. Kevlar straps, which extend through the EA, stabilize each EA.

Typical lightweight pneumatic methods include internal and/or external air bladders and both methods have been demonstrated successfully in this study. An example of an external air bladder system is shown in Figure 10, where the deployment bladder, secured on the impact surface of the EA, also serves as a cover needed to transfer the impact loads into the cell-walls in case of soft soil, or water impact. An advantage offered by the external bladder method when compared to internal bladders is higher deployment speed. Furthermore, this method is compatible with existing airbag deployment hardware. An obvious disadvantage, however, is lack of retraction capability in case of an aborted incident.

3. Energy Absorber Design and Optimization

Design tools for the tailoring of composite cellular structures have been utilized by Kellas [10-12] who employed theory that was previously developed for isotropic cellular structures by Abramowicz, Wierzbicki and their co-workers [13-18]. This type of theoretical treatment requires the cross-section of the cellular structure to be regarded as being composed of an assemblage of basic elements such as "Y", "T" and "+".

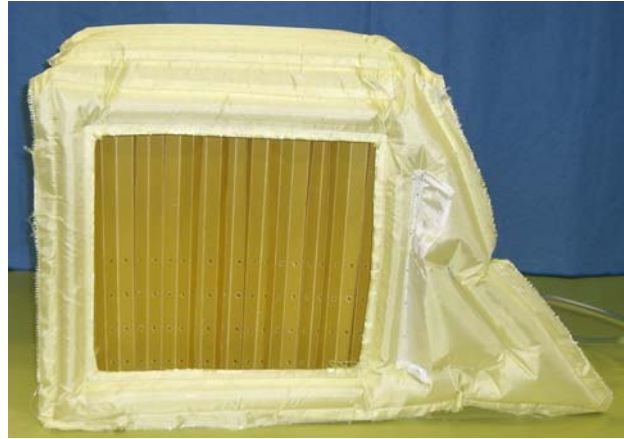


Fig. 10. Expanded EA with integrated cover system. Deployment was achieved by simply inflating the bladder to approximately 1.5 psi. Straps could be combined with this system for additional global stability.

The sustained crush load for a single element is estimated from the total energy balance of input (applied-load times crush-displacement) and absorbed energy (sum of all energy dissipation modes such as folding, stretching, tearing, delamination, etc.). For cellular structures made of ductile materials, there are three basic modes of energy dissipation. These include extensional deformation at the center of the deformed element, folding at stationary horizontal hinges, and folding and unfolding due to moving inclined hinges [13-18]. A typical deformation mode for a "Y" element is shown in the schematic of Figure 11.

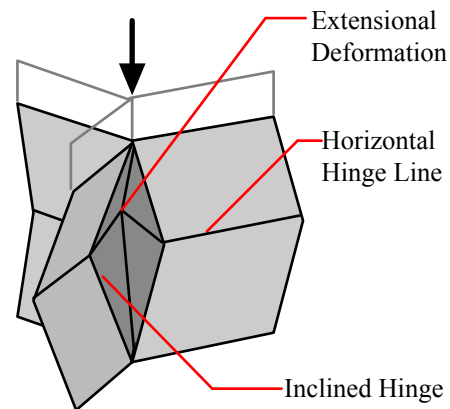


Fig. 11. Energy absorbing deformation modes for "Y" element of conventional honeycomb.

It has been shown [10-12] that composite cellular structures can be treated using the same theory [13-18] as long as the cell-walls are designed to deform quasi-plastically and energy is absorbed in a similar way to that of metal cellular structures. One obvious difference between the deployable and conventional honeycombs is the flexible hinge. While the effect of the flexible hinge on the energy dissipation cannot be quantified without detailed analysis, it is

anticipated that the flexible hinge could lead to lower energy absorption. Differences between conventional and deployable honeycombs can be assessed using the theory of Wierzbicki [15] to predict the crush strength of conventional honeycombs with similar cell-wall properties as those of deployable structures. Such a comparison is depicted in Figure 12 for three deployable structures of the same cell-wall, a single woven ply of Kevlar-129, and different cell widths ($W = 0.75''$, $1.0''$ and $1.25''$).

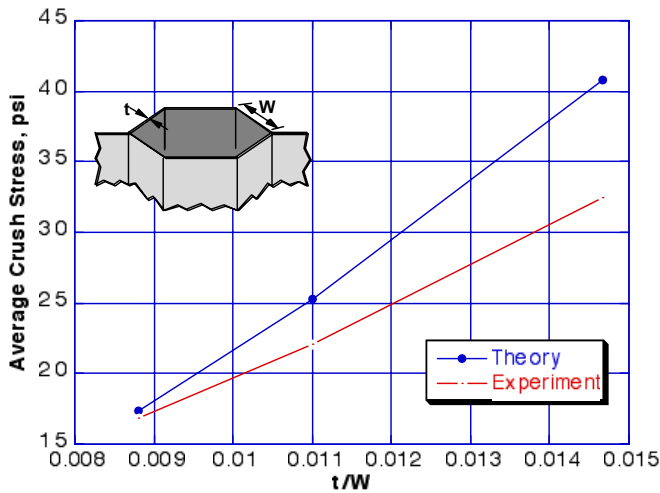


Fig. 12. Average sustained crush stress versus t/W . Theoretical points were derived using the relationship of stress versus t/W , as described in reference [15].

While similar trends are shown in Figure 12, there are at least two differences between theory for conventional honeycombs [15] and the measured response of the deployable samples chosen for this study: (a) lower measured strength and (b) shallower experimental stress/ (t/w) slope. Inspection of the folding mechanisms, depicted in Figure 13, shows that the extensional deformation mechanism (Figure 11) is not present. Instead, for the deployable composite sample shown in Figure 13, energy is absorbed primarily through the formation of hinge lines and localized delamination to accommodate compatibility. Since extensional deformation is a more efficient mode of energy dissipation, it is anticipated that a better choice of adhesive to minimize delamination and promote stretching and/or tearing can lead to improved energy absorption.

In addition to the folding differences, other contributing factors to the lower experimental strength compared to theory include EA overall size and cell-wall perforation effects. Samples used in these tests were of finite width and depth, and, as such, are subject to much lower strength due to the weaker cells along the boundary (perimeter). An example of EA size effect is highlighted in Figure 14 where an increase in average crush stress of approximately 20% is

evident when the cell count of otherwise identical deployable samples was increased from 59 to 104 cells.



Fig. 13. Post-crush photograph of a deployable honeycomb made of Kevlar-129.

Furthermore, early in this program it was made clear that perforations were needed to relieve internal air pressure, which builds up as the sample is crushed rapidly. Dynamically tested samples without vent holes exhibited partial cell blow-out and hence reduced energy absorption during the last portion of their stress/stroke response as indicated by the 59-cell sample in Figure 14.

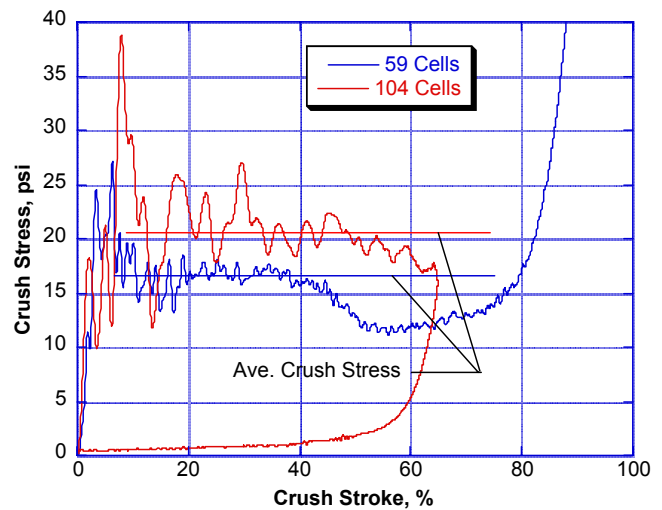


Fig. 14 Dynamic crush response of deployable honeycomb samples with similar cell geometry. Both samples were made of a single woven layer of Kevlar-129.

As with all aerospace structures, specific properties are of primary interest. Therefore, for the deployable honeycomb a parameter that needs to be optimized is average crush stress over energy-absorber expanded density. When a honeycomb is expanded linearly to its optimum shape, the resulting

volume can be up to two orders of magnitude larger than its packed volume depending on the cell geometry (cell cross section, cell-wall width W , and cell-wall thickness t). Theoretically, the ratio of the expanded over the packed volume for linearly expanded cellular structures is approximately equal to $0.65/(t/W)$ and $0.25/(t/W)$ for hexagonal and square cross section cells, respectively. Thus, a greater volumetric ratio can be achieved either by increasing the cell width for a given thickness or by reducing the cell-wall thickness for a given cell width. Another factor that influences the expanded density of the energy absorber is the mode of expansion, with linear providing up to two times greater volumetric efficiency compared to radial expansion.

A typical trend of experimental specific crush strength versus the ratio, t/W , is shown in Figure 15. The figure highlights the advantage of using a higher cell-density sample in order to maximize the amount of energy absorbed relative to energy-absorber expanded density.

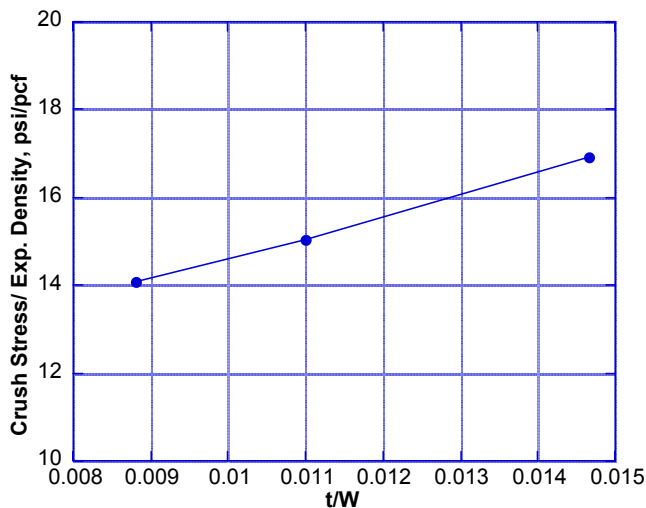


Fig. 15. Relationship between experimentally measured specific crush strength and t/W . All three values represent dynamic data at approximately 20 fps impact velocity.

While the energy absorber sustained crush stress is primarily controlled by factors such as the cell-wall yield strength, cell geometry (t/W), and hinge strength, the initial peak can be tailored by shaping the impact surface of the energy absorber. Another effective option for initial peak load regulation is cell-wall tapering where cell-walls are fabricated thinner or weaker at the surface of the energy absorber. For multi-ply composite structures this could be achieved by simply discontinuing some of the plies close to the surface.

4. Static and Dynamic Tests

Various static and dynamic tests were performed including component tests to verify, amongst other factors, fabrication

materials and techniques, and full-scale tests where a complete set of energy absorbers was tested.

4.1 Component Tests

Component tests were performed as needed to better understand the behavior of the deployable structures. Such tests included:

- (a) static and dynamic tests of energy absorber sections to evaluate fabrication methods and materials,
- (b) off-axis dynamic tests on energy absorber sections to assess the effect of cell axis orientation with respect to the applied load on the crush strength,
- (c) dynamic tests on energy absorber sections to evaluate the effect of geometric parameters (cell wall thickness, cell wall width, perforation pattern, and number of cells) on the sustained crush stress and total energy absorption capacity,
- (d) static tests on individual cells to investigate the effect of cell size on the apparent shear buckling (strength),
- (e) static tests on cell-wall material to obtain material properties for mathematical models and,
- (f) tests on various deployment and tie down methods.

Among other parameters, the sustained crush stress and shear stability are important parameters that define the performance of the deployable energy absorber. The sustained crush stress is measured very easily using a drop test. However, measuring (or estimating) the global shear stability of the deployable structure is not as simple a task. For this study, two indirect approaches of evaluating the shear stability of the deployable structures were used. In both cases relatively simple tests were devised where shear instability was promoted. These tests were then simulated using LS-DYNA to calibrate the material models by adjusting the input values. More detailed information on the dynamic modeling approach is presented in a separate section of the paper.

In the first approach, shear stability was evaluated through crushing of otherwise identical sections with cell axis orientation to the loading axis of 0° , 14° and 27° . Samples for this study consisted of a hybrid (glass/spectra) cell-wall (total thickness 0.016") and each contained a total of 41 cells. The specimen height (measured vertically) was 7.3", 6.1" and 6.0" for 0° , 14° and 27° respectively. The dynamic crush response for each of these samples is shown in Figure 16. Recognizing the fact that the crush response of the off-axis samples will depend on height, no general conclusions can be made based on the off-axis crush results. However, by modeling each test and adjusting the input shear properties until each response is matched, useful global stability information was obtained.

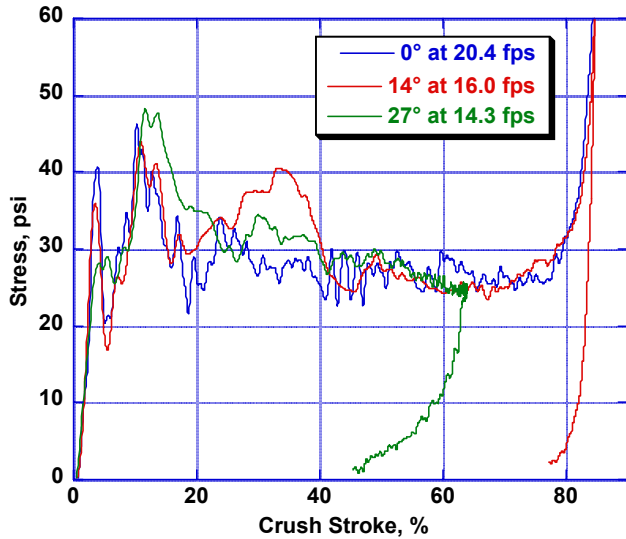


Fig. 16. Effect of cell-axis orientation on the crush response of spectra/glass hybrid deployable honeycombs. All samples had the same cell-wall thickness and width.

It is evident, from Figure 16, that the sustained crush stress is approximately the same for all three samples despite the increased shearing present in the off-axis samples as shown in Figure 17 which depicts three frames from a high speed video of the actual 27° off-axis crush test.

The effect of cell geometry on the shear stability was studied through a series of simple, quasi-static tests. Three-point-bend tests were conducted on single-cell samples. Specimens were fabricated using the same materials and methods as the actual deployable structures, including hinge lines. A typical test sample, under load, is shown in the photograph of Figure 18. Each cell sample contained three hexagonal Bakelite stanchions located at each of the loading points. The role of the stanchions, which were bonded to the cell-walls, was to preserve the hexagonal shape of the cell while distributing the load uniformly over the entire perimeter of the cell. To eliminate possible trapped air effects during loading, each stanchion was perforated. The test fixture, shown in Figure 18, was designed to accommodate samples of varying length L and load/displacement data were recorded until a peak load was reached. Typical load/displacement responses from this study are shown in Figure 19 and a summary of all results, as maximum stress versus t/W , is shown in Figure 20. Note that for all specimens, the ratio L/W was kept constant at 1.75.

Characteristic instability modes in this type of sample were shear buckling in the lower oblique cell-walls and compressive buckling on the top horizontal cell-wall as indicated in Figure 18. Due to considerable scatter in the results, as shown in Figure 19, at least five samples were tested for each geometry case. The maximum stress was

calculated using the peak load divided by the cross sectional area of the hexagonal cell. The cross-sectional area of the flanges (flaps) was neglected. Each datum in Figure 20 represents the average from at least five samples.

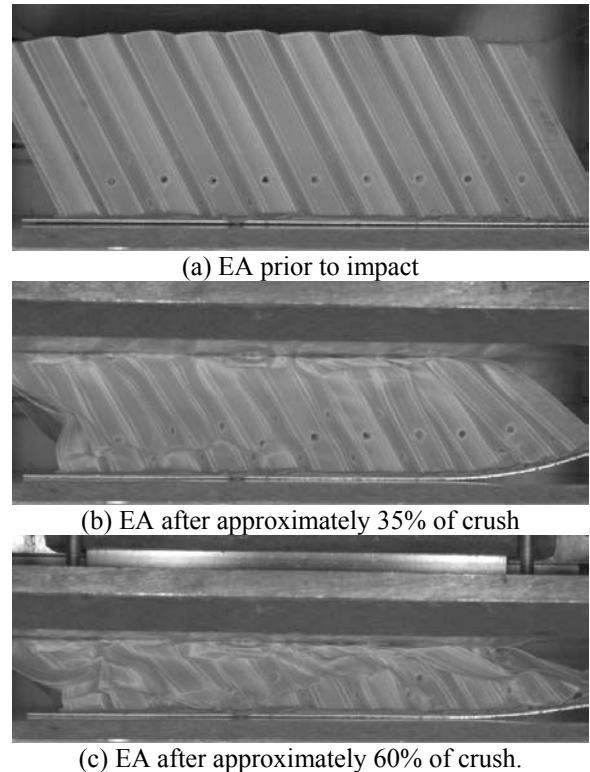


Fig. 17. High speed video frames from 27° off axis test.

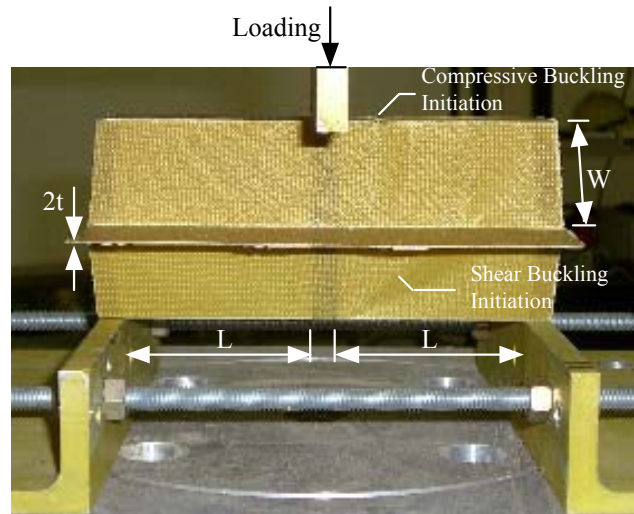


Fig. 18. Three-point-bend set-up for single cell tests. For the sample shown, $W=1.5''$ and $t=0.010''$. The flange thickness was $2t$.

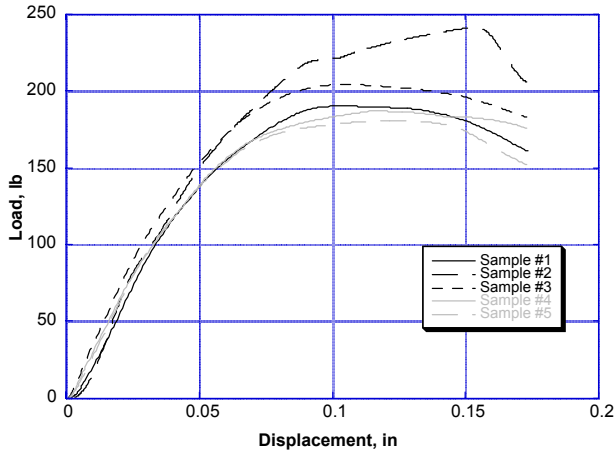


Fig. 19. Load displacement response from 3-point-tests on samples with $t=0.010''$, and $W= 1.0''$.

According to Figure 20, and assuming that the three-point bend test is a true representation of shear stability, the shear stability (like the sustained crush stress) also increases with t/W .

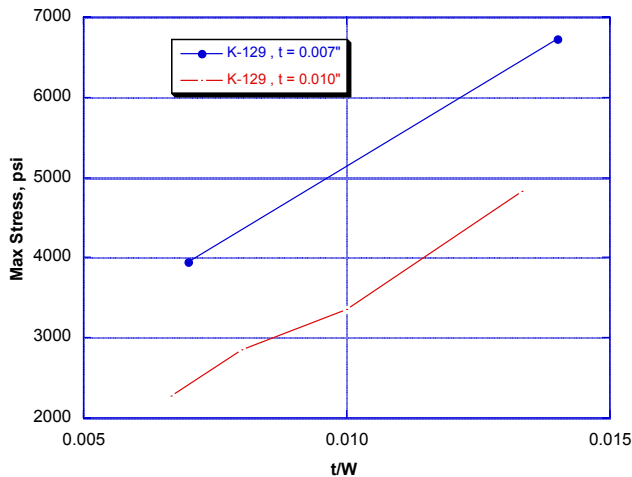


Fig. 20. Peak stress as a function of t/W for hexagonal cells made of two Kevlar 129 fabrics ($t=0.01''$ and $0.007''$).

4.2 Full-Scale Tests

For the first full-scale demonstration test, a composite (5 ft in diameter) fuselage section was utilized. To ensure fuselage survivability for use in subsequent tests the open section was stiffened by a pair of $\pm 45^\circ$ woven glass straps as shown in Figure 21. Four deployable energy absorbers were fitted to the test section as shown in Figure 21 and dropped on a concrete surface at 38.4 fps. The suspended fuselage prior to test is shown in Figure 22. The total fuselage weight (including the weight of ten 100-lb lead blocks) was 1,212 lb. Lead blocks were secured onto the fuselage floor through standard seat rail fasteners. The energy absorbers were made of a single woven-ply of Kevlar 129 and weighed 5.6 lb each. Each EA was 20'' tall, 16.5'' wide and 20.5'' deep.

Vertical accelerations were measured at six locations on the fuselage floor with accelerometers mounted in the center of selected lead blocks (one accelerometer at each of four corner lead blocks and one accelerometer at each of two center blocks). Acceleration/time histories were used to calculate crush displacements through double integration. As one would expect of a nearly flat impact all acceleration time histories were similar to each other. The acceleration/stroke response from one of the central floor locations is shown in Figure 23.



Fig. 21. Photograph of composite fuselage section with energy absorbers installed. A radius of curvature of approximately 18'' was machined in each EA to attenuate the initial peak load.



Fig. 22. Photograph of composite fuselage section suspended from the drop tower portal at the actual test drop height and a nominally flat attitude. The impact velocity was 38.4 fps.

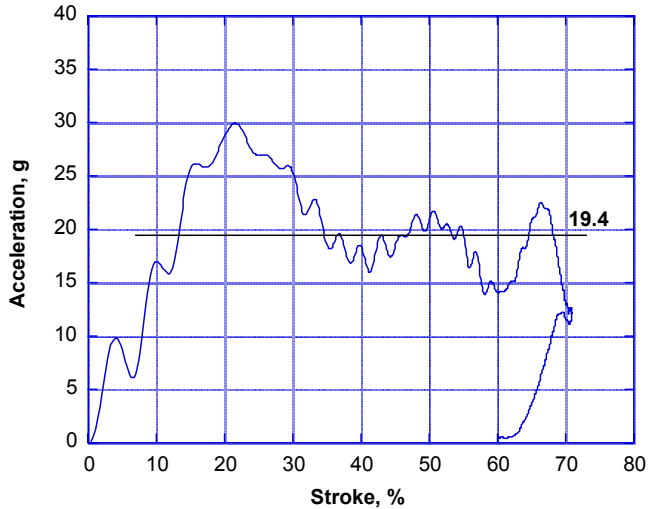


Fig. 23. Typical acceleration/stroke response from the vertical fuselage test: – center left accelerometer.

The energy absorbers for the vertical fuselage test were sized for a 20-g level. As with most high speed impacts, the acceleration/stroke response of Figure 23 shows that the 20 g level was exceeded during the initial part of the crush. Additional initial pulse attenuation would have been possible by a more aggressive shaping of the energy absorbers. For this test, EAs were shaped with a single curvature of 18” radius.

Both high-speed video coverage of the test and the acceleration/stroke responses showed that the majority of the fuselage’s kinetic energy was managed effectively by the energy absorbers which crushed progressively to approximately 70% of their 85% stroke capability.

The second full-scale demonstration test involved oblique impact on concrete. For this test energy absorbers with tapered cells were fabricated and the fuselage section from the first test was modified to accommodate the radially expanded energy absorbers as shown in Figure 24. The fuselage section is shown in Figure 25 suspended from the drop tower portal at the impact attitude prior to test.

All four energy absorbers were hinged at the outer edge, and when expanded, were held in place by a set of Kevlar straps that extended through each energy absorber. The same materials used in the fabrication of the first set of energy absorbers were also used for the second test. However, to accommodate the fuselage curvature, the cell geometry was varied from W=1.0” hexagon at the impact surface to 0.8” by 2” rectangle at the base. Each energy absorber was 24” long 18” wide and 30” deep at the impact surface and weighed approximately 9.5 lb. A larger volume of energy absorber was used to account for the fact that, during initial impact, only one energy absorber was engaged.



Fig. 24. Photograph of composite fuselage section with four energy absorbers: – two of the EA are shown in the packed position. The fuselage section is photographed upside down.

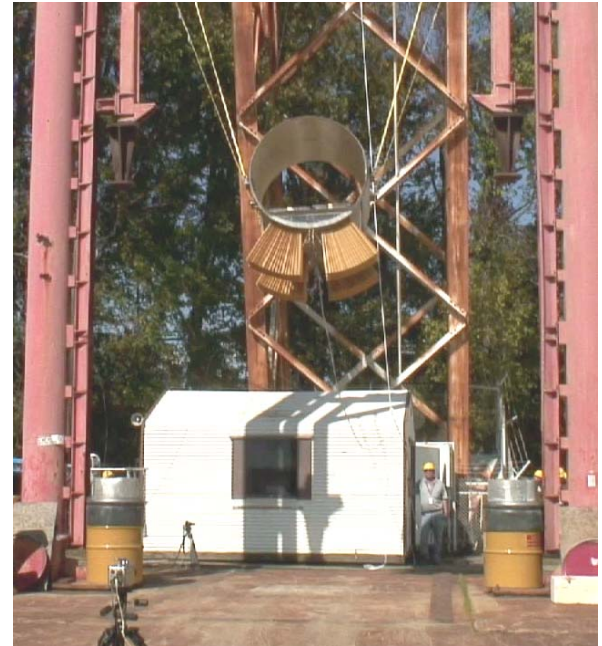


Fig. 25. Photograph of composite fuselage section suspended from the drop tower portal at the actual test drop height and intended attitude of 6.7° pitch and 3.2° roll. Vertical impact velocity was 28.3 fps.

Due to better than anticipated performance of the energy absorbers during the first full-scale test, it was thought that

stiffening of the open section during the second test was unnecessary and the woven glass straps were removed.

Acceleration/time responses from three mutually perpendicular accelerometers located at the center of the floor are shown in Figure 26. These indicate that the linear accelerations were well within the desired 20-g allowable level. High-speed video records of the oblique impact test showed that the energy absorbers performed in the desired fashion. However, improvements to the tie down methods could increase the performance even further.

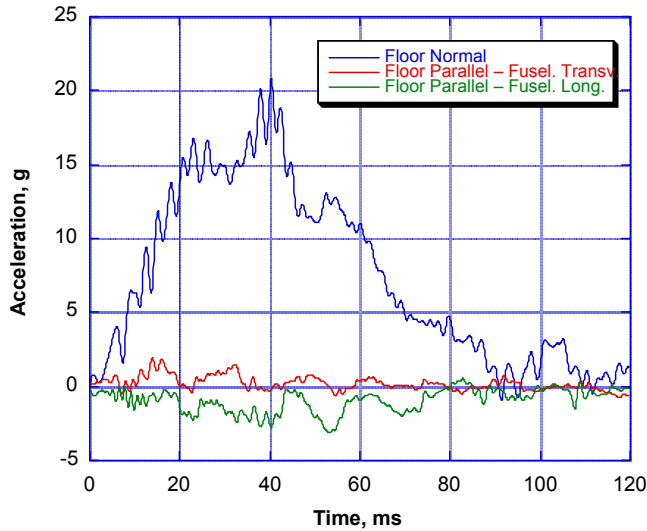


Fig. 26. Acceleration/time response for oblique fuselage-section drop. The three orthogonal accelerometers were mounted at the center of the floor.

5. Computer Simulations

Two types of computer simulations were performed using the nonlinear, explicit transient dynamic finite element code, LS-DYNA [19]. The first simulation consisted of modeling the three-point-bend test of a single cell specimen with the objective of optimizing material input properties through model calibration. Verified material properties obtained from the single cell simulations will be used as input to more elaborate simulations of the composite energy absorbers. The second simulation was an LS-DYNA model of the composite fuselage section outfitted with four EA blocks that was impacted at 38.4-ft/s onto a rigid surface. Descriptions of both types of simulations are presented in this section of the paper.

5.1 Three-Point Bend: Single Cell Model Description

Even though the single cell specimen was loaded quasi-statically, the simulation was executed using LS-DYNA v971 for the sole purpose of verifying the material input properties for “MAT_58”, which will be used in future simulations of the energy absorber. A picture of the

complete model is shown in Figure 27. The model consists of three major parts: the “Bakelite” stanchions, the hexagonal-shaped deformable composite cell-wall, and the flanges. These parts are shown separately in Figure 28. The cell dimensions were cell-wall width (W) = 0.75”, cell-wall thickness (t) = 0.010” and overall length equal to 3.35”. The model was constructed using an element edge length of 0.05”.

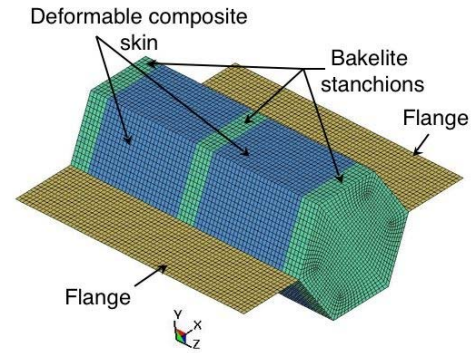


Fig. 27. LS-DYNA single cell model for 3-point-bend test.

The Kevlar cell-wall was represented using *MAT_58 [20] or *MAT_LAMINATED_COMPOSITE_FABRIC in the LS-DYNA model. Data from tensile tests of $0^\circ/90^\circ$ coupons were used to determine approximate values of modulus and failure strain in both the longitudinal and the transverse directions. Likewise, data obtained from tensile tests of $\pm 45^\circ$ coupons were used to estimate the shear stiffness and strength [21]. The flanges consisted of two layers of Kevlar fabric, with a total effective thickness of 0.02” as indicated in Figure 28. The thickness of the adhesive layer in the flanges was neglected. The specific material properties used in the model to represent the Kevlar 129 fabric are shown in Table 1. The Bakelite stanchion was represented using a linear elastic material with a density of $1.356E-4$ lb-s²/in⁴, an elastic modulus of $1.09E+6$ psi, and a Poisson’s ratio of 0.25. The complete model consisted of 27,582 nodes; 16,840 hexagonal solid elements; and 8,040 Belytschko-Tsay shell elements. As shown in Figure 28, only three parts were defined.

The test specimen was loaded in three-point bending by applying a compressive load at the center of the hexagonal cell using a 0.25” wide pad as shown in Figure 18. In the test, loading was performed in displacement control with a loading rate of 2.0 ipm. The reaction points (0.25” from the bottom edge) were assumed to be simply supported. To represent the simply supported boundary conditions, a *BOUNDARY_SPC_SET was defined in the model. For this set, all of the nodes within the 0.25” by 0.75” area at the bottom of both ends of the specimen were constrained from linear motion in the x- and y-directions. The nodes were free to move in the z-direction, and free to rotate in all

directions. Note that the axis directions are shown in Figure 27.

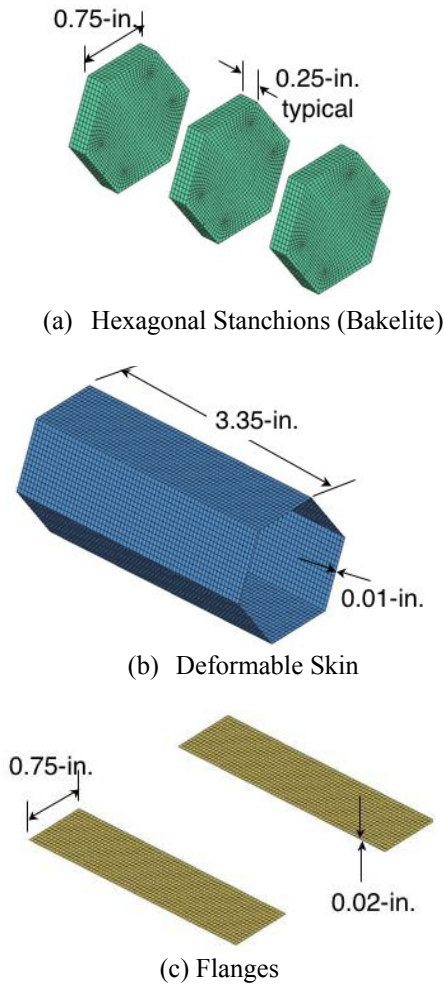


Fig. 28. Three distinct parts of the LS-DYNA model.

To represent the three-point loading condition, all of the nodes within the 0.25” by 0.75” loading area at the center of the cell were assigned a *LOAD_NODE_SET condition. This condition specified that at 0.0 seconds the load was 0.0 lbs. At the termination time, the maximum load was 2.8646 lb. Note that 2.8646 lbs times 96, which is the number of nodes included in the set, equals 275 lbs., which is slightly over the maximum load observed in the test. Simulations were conducted in which the end time was varied in discrete intervals from 0.001- to 1.0-seconds. For these simulations, the end time serves as a scale factor for the load. For shorter end times the load is applied more rapidly. For longer end times the load is applied slowly, mimicking the quasi-static loading condition used in the test. A plot of failure load versus end time is shown in Figure 29. The failure load was determined by finding the time at which the first element failure occurs. This time is multiplied by 275 (maximum load) and then divided by the termination, or end time of the simulation. The plot shown in Figure 29 indicates a sudden

decrease in failure load as the end time increases from 0.001- to 0.05-second. For end times greater than 0.05 second, the failure load remains constant at 228 lb. Obviously, the end time is an important factor in this simulation. As shown in Figure 29, longer end times provide stable and consistent results. However, the CPU time required to execute simulations with longer end times can become intractable. In fact, the simulation with an end time of 0.5 seconds required 112 hours of CPU time.

Table 1. Material properties used in the LS-DYNA model to represent the ±45° Kevlar 129 fabric.

Material Property	*MAT_58
Density, lb-s ² /in ⁴	1.29E-4
Young's modulus longitudinal direction, psi	2.7E+6
Young's modulus transverse direction, psi	2.7E+6
Poisson's ratio	0.3
Stress limit of nonlinear portion of shear curve, psi	4,000.0
Strain limit of nonlinear portion of shear curve, in/in	0.0187
Shear modulus, psi	307,481.0
SLIMT1	0.8
SLIMC1	1.0
SLIMT2	0.8
SLIMC2	1.0
SLIMS	0.25
ERODS	0.1
Strain at longitudinal compressive strength, in/in	0.035
Strain at longitudinal tensile strength, in/in	0.05
Strain at transverse compressive strength, in/in	0.035
Strain at transverse tensile strength, in/in	0.05
Strain at shear strength, in/in	0.05
Longitudinal compressive strength, psi	56,000.0
Longitudinal tensile strength, psi	80,000.0
Transverse compressive strength, psi	56,000.0
Transverse tensile strength, psi	80,000.0
Shear strength, psi	7,500.0

5.2 Three-Point Bend: Test/Analysis Correlation

As described in Section 4, the three-point-bend study for 0.01” thick cell-walls involved four scaled (same L/W) cases (W= 0.75”, 1.0”, 1.25” and 1.5”). Since specimens were scaled, only one was chosen for simulation and correlation with experiment.

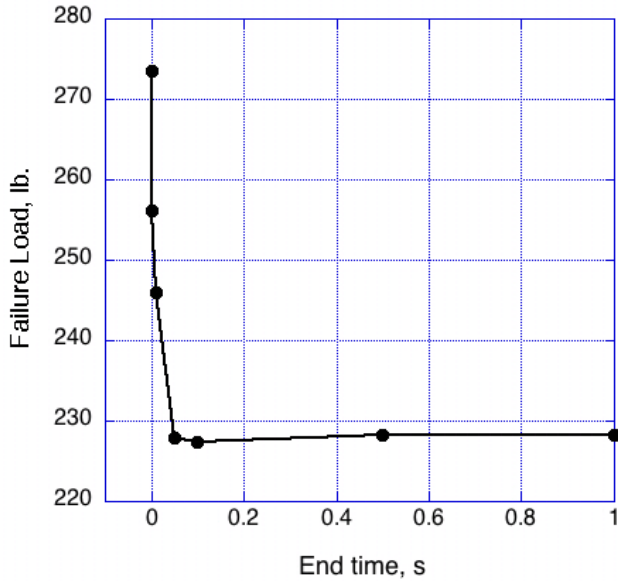


Fig. 29. Failure load versus end time for three-point-bend test.

Test and analysis plots of load versus displacement are shown in Figure 30 where the experimental scatter is bounded by the two extreme curves (dark shaded region). Note that only the data up to maximum load are shown. During the experiments, a complex unloading response was also recorded. For the analysis, the load displacement curves for the simulations with end times of 0.01- and 0.1-seconds are plotted using dashed lines. A light gray band is formed between the two analytical curves.

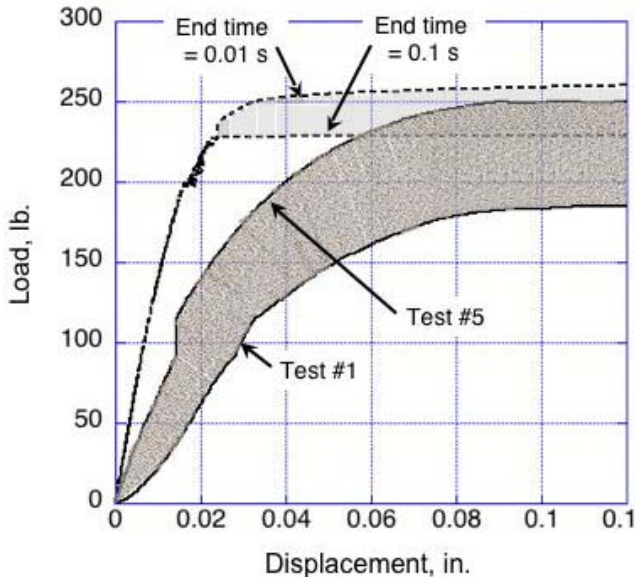


Fig. 30. Test/analysis correlation for three-point-bend test ($W=0.75''$, $t=0.01''$).

As indicated in Figure 30, the initial predicted response is much stiffer than the experimental response, which is

nonlinear. However, once the maximum load is achieved, the analytical and test bands intersect. The analytical curve with an end time of 0.1-second falls within the experimental scatter band, whereas the curve representing an end time of 0.01-second is completely outside of the experimental band. The failure load for the LS-DYNA 0.01-second simulation is well above the stable load exhibited by simulations with end times equal to 0.05- through 1.0-seconds, as shown in Figure 29. These results indicate that the failure properties assigned to the deformable skin are correct and give reasonable comparisons with test data. However, the initial nonlinear portion of the experimental curve is not well predicted.

Following the first element failure, the model essentially collapses, exhibiting no post-buckling behavior. Initial failure is depicted in Figure 31, which shows fringe plots of History Variable #3 up to maximum failure load for the 0.1-second simulation. History Variable #3 represents a cumulative damage parameter for shear associated with the deformable skin which is modeled using the *MAT_58 card.

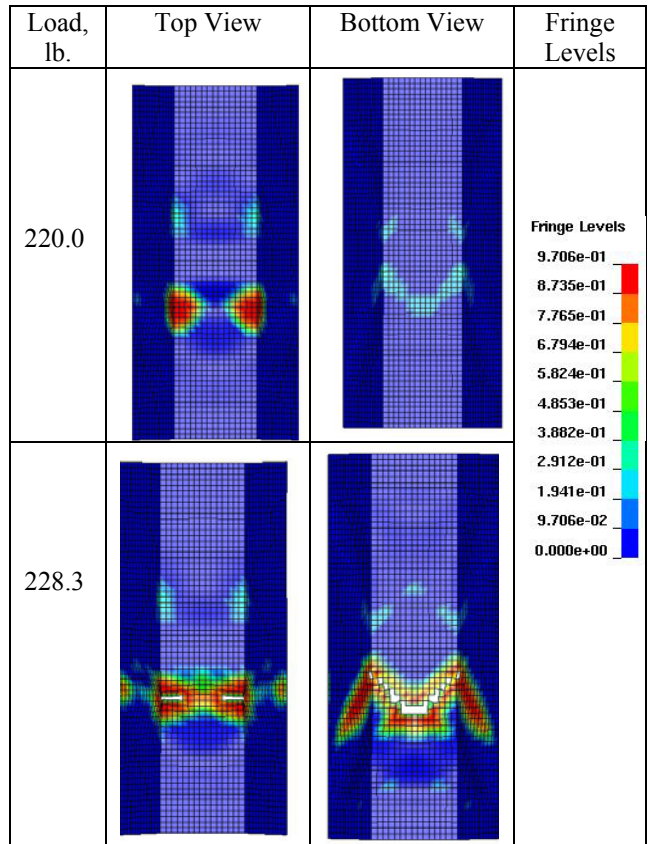


Fig. 31. Fringe plots of history variable #3.

In three-point bending, the top surface is subjected to compressive loads, while the bottom surface is subjected to tensile loads. Regions of high damage are shown in red. At a load of 228.3 lb, both the compressive and tensile surfaces show element failures. LS-DYNA removes failed elements

from the simulation. As a result, total collapse of the model occurs at the next load increment. Conversely, the test specimens exhibit initial instability in the form of shear and compressive buckling, as shown in Figure 18, and subsequent delamination that spreads into the flange regions. The specimens do not collapse after maximum loading is achieved and exhibit a complex unloading response.

5.3 Fuselage Section: Test-Article Description

A finite element model was developed to represent the composite fuselage section that was retrofitted with four composite honeycomb energy absorbing blocks. LS-DYNA simulations were executed to simulate the 38.4-ft/s vertical drop test of this fuselage section that was conducted onto a rigid surface in August 2006 at NASA Langley Research Center. The composite fuselage section was developed during a three-year research program in the late 1990's and has since been used as a test bed to evaluate structural scaling effects, multi-terrain impacts, seat and occupant loadings, and model correlation studies [22-31]. A pre-test photograph of the test article is shown in Figure 21. The fuselage section is 5-ft. in diameter and is approximately 5-ft in length. The upper cabin of the fuselage is a composite sandwich construction with a 3-lb/ft³ closed cell polyurethane foam core and E-glass/epoxy fabric face sheets. The sandwich floor of the fuselage consists of an 8-lb/ft³ closed-cell polyurethane foam core with hybrid face sheets consisting of E-glass/epoxy and graphite/epoxy composite fabric. The layers of graphite/epoxy fabric and the higher density foam were used for increased stiffness and improved structural rigidity of the floor.

Standard aircraft seat tracks were mounted to the floor of the fuselage section, to the left and right of the centerline. Ten 100-lb. lead masses were attached to the seat tracks, five per side, to represent typical floor loading provided by seats and occupants, as shown in Figures 21 and 32.

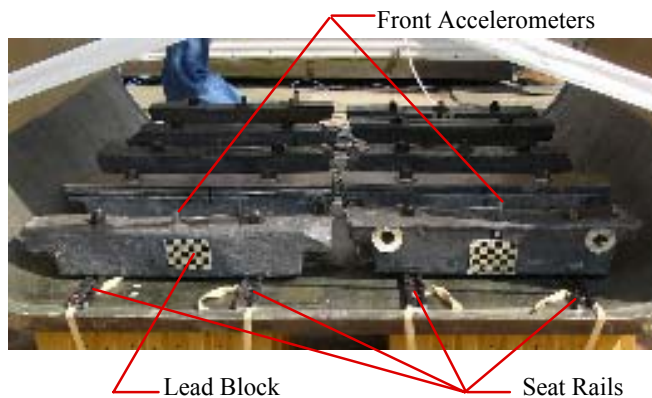


Fig. 32. Close-up photograph of fuselage floor showing instrumentation position, the seat rails and lead blocks.

Four deployable energy absorbers were attached beneath the floor of the section, as shown in Figure 21. The energy

absorbers were located symmetrically about the centerline and mid-plane of the fuselage section.

5.4 Fuselage Section: LS-DYNA Model Description

The LS-DYNA version of the finite element model that is documented in Reference 31 was modified for this simulation by removing the original subfloor and the lower skin surrounding the subfloor, leaving only the upper cabin and floor. A picture of the model is shown in Figure 33. The model contains: 51,860 nodes; 13,413 Belytschko-Tsay shell elements; 39,074 hexagonal solid elements; 188 beam elements; 40 element masses; 14 parts; and 8 material properties. The shell elements are used to represent the inner and outer skins of the composite sandwich and the impact surface. The solid elements represent the upper cabin foam-core, the floor foam-core, and the composite energy absorber, which in this preliminary analysis was represented as crushable foam. The beam elements represent the seat tracks that were mounted to the floor. Concentrated element masses were used to represent the 100-lb. lead masses that were attached to the seat tracks. An automatic contact was used to define contact between the nodes in the model and the impact surface. The edge nodes of the impact surface were fixed using a nodal constraint definition.

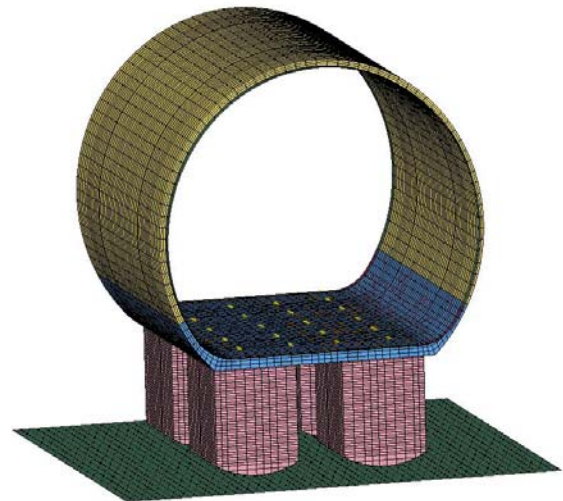


Fig. 33. LS-DYNA finite element model of the vertical fuselage drop test.

Eight different material properties were defined in the model. The material properties of the E-glass/epoxy and the graphite/epoxy fabric materials were determined from coupon tests and are represented using a bilinear elastic-plastic material model with strain hardening. The 3- and 8-lb/ft³ polyurethane foam cores were modeled as linear elastic solid materials. The laminate stacking sequences of the multi-layered face sheets were defined using the *SECTION_SHELL card with *INTEGRATION_SHELL used to specify the layer thicknesses and the number of integration points. The energy absorbers were modeled

using *MAT_63 or *MAT_CRUSHABLE_FOAM with a curve of stress versus strain data input to define the crush response. The stress-strain data were determined from a component test performed at 22.2 ft/s velocity. A plot of the experimental data and the fitted response that was input to the model is shown in Figure 34. Also, note that a *MAT_ADD_EROSION card was specified for this material. This card established the strain (0.85 in/in) at which an element within the energy absorbing blocks would be eliminated from the model. Finally, it is worth noting that the unloading curve for this material definition is elastic, i.e. the unloading curve is a straight line that initiates at the point of unloading and is parallel to the initial compressive response. However, the experimental data shown in Figure 34 indicate that the actual unloading curve is hysteretic. The model was executed for 0.15 seconds using LS-DYNA v971, which required 7 hours and 30 minutes of total CPU time.

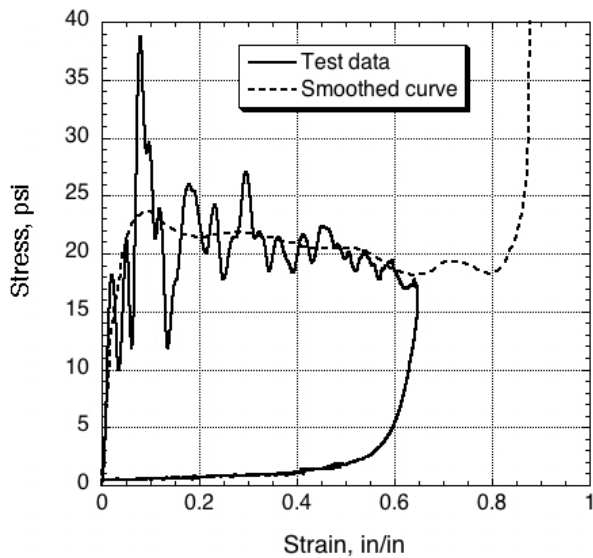


Fig. 34. Input data for the EA crush response.

5.5 Fuselage Section: Test/Analysis Correlation

The test-analysis correlation is presented in two parts: a comparison of structural deformation and a comparison of acceleration-, velocity-, and displacement-time history responses. The deformed model and test article are shown in Figure 35 for two discrete time intervals. At both time steps, the upper cabin of the fuselage section exhibits some elastic deformation evident in both the model and the test article. However, significant differences are observed in how the energy absorbing blocks behave during impact. For the test, the cell walls within the composite honeycomb structure fold sequentially forming an accordion-like deformation pattern. Following the impact event, elastic energy, which is a small portion of the total energy, is released providing some rebound velocity. Conversely, the energy absorber in the model shows element compression initiating in the area of

contact with the impact surface. In addition, some minor crushing is seen at the top of the foam blocks. Early in time, the crushing and compression of the solid elements occurs in a stable manner; however, eventually the block buckles as a result of uneven compressive loading. Very little rebound of the model is observed.

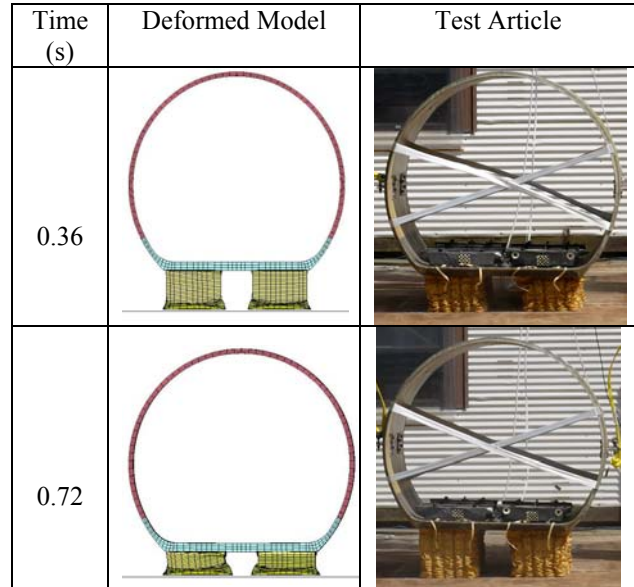


Fig. 35. Analysis and test comparisons of EA crush.

As expected, the solid element representation of the energy absorber does not provide the accordion-like deformation pattern observed in the experiment. In agreement with experiment, no damage was predicted or observed in the upper cabin or floor of the fuselage section.

Analytical and experimental comparisons of acceleration-, velocity-, and displacement-time-histories are plotted in Figures 36, 37, and 38, respectively, for the center lead mass on the right side. The experimental acceleration curve, shown in Figure 36 was filtered at 0.5kHz and the analytical acceleration curve was filtered using the SAE Channel Filter Class (CFC) 180 [32]. The analytical acceleration response shows excellent agreement with the experimental curve for the first 0.03 seconds, accurately predicting the magnitude and timing of the peak acceleration (30-g). Following the initial peak, the model predicts two additional peaks of lower magnitude (25-g) than the first. At 0.06 seconds, the predicted acceleration falls off sharply to 0-g. Each of the three peaks seen in the predicted response is associated with the collapse of a group of compressed solid elements in the energy absorbers.

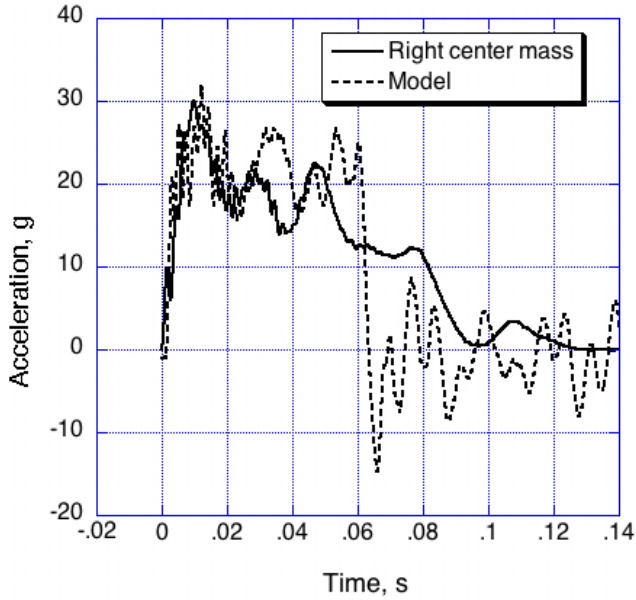


Fig. 36. Acceleration time history comparison between analysis and experiment.

The experimental acceleration response also exhibits three distinct peaks. The first peak occurs at 0.01 seconds and has a magnitude of 30-g. The second peak occurs at 0.028 seconds and has a magnitude of 21-g and the third peak occurs at 0.047 seconds with a magnitude of 22-g. Following the third peak, the magnitude of the experimental acceleration decreases gradually over the next 0.052 seconds to 0-g. Due to the sudden drop in the acceleration response and the relatively short pulse duration, the average acceleration of the predicted response is 22.7-g. Conversely, the experimental acceleration response has longer pulse duration and an average acceleration of 19.4-g.

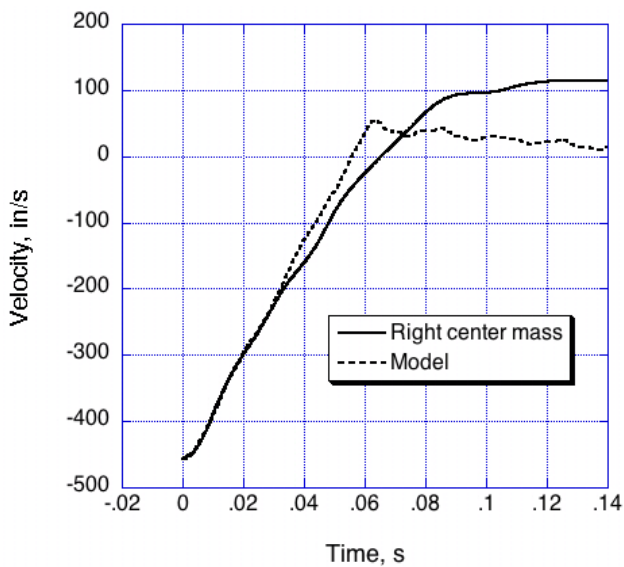


Fig. 37. Velocity time history comparison between analysis and experiment.

Note that the analytical and experimental acceleration time-histories of the right center lead mass are typical of the responses seen for the other lead masses for which test data were obtained.

A comparison of the experimental and analytical velocity time histories is shown in Figure 37. These curves were obtained by integration of the corresponding acceleration responses shown in Figure 36. As expected, a high level of correlation is observed for the first 0.03 seconds. After that time, the two curves deviate from one another with the analytical curve removing velocity more quickly than the test. The analytical velocity response crosses zero at 0.055 seconds and exhibits a rebound velocity of 51 in/s at 0.062 seconds. The rebound velocity is reduced nearly to zero by the end of the pulse. Conversely, velocity was removed more slowly for the test, and achieves a maximum rebound velocity of 113 in/s at 0.12 seconds.

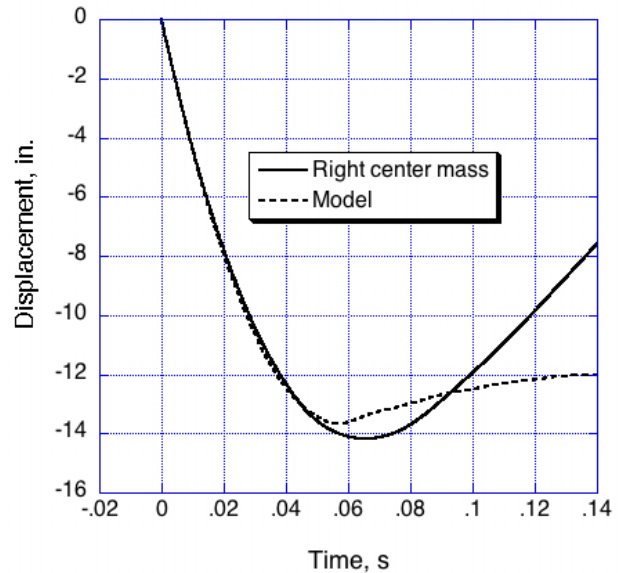


Fig. 38. Displacement time history comparison between analysis and experiment.

Finally, the velocity responses shown in Figure 37 were integrated to provide experimental and analytical displacement time-histories, which are plotted in Figure 38. The displacement curves show excellent agreement up to 0.05 seconds. After that time, the predicted displacement curve levels off and achieves a maximum displacement of 13.7” at 0.056 seconds. Meanwhile, the test curve continues to displace vertically downward to a maximum of 14.25” at 0.066 seconds.

6. Discussion of Results

6.1 Experimental Work

All energy absorbers used in this study were fabricated with off-the-shelf materials and no attempt was made to optimize the structural response through specialized reinforcements and/or adhesives. It is anticipated that 10 to 20% improvement in properties such as specific energy absorption can be realized by simply replacing the 0.01" thick layer of adhesive used in the fabrication of the deployable honeycomb energy absorber.

Other possible improvements include perforation patterns to maximize venting without weakening the cell walls, and more effective tie downs to improve shear stability. So far as deployment is concerned, the most promising method appears to be the combination of external inflatable bladder (integrated cover) and tie down straps. This method is particularly suited to rapid deployment, necessary for aircraft crashworthiness applications while providing the added benefit of functional multi-terrain impact capability.

Results from the successful vertical drop test of a retrofitted composite fuselage section indicated that the energy absorbers removed almost all of the kinetic energy of the impact event. Despite the 38.4-fps impact velocity, no damage to the upper cabin or floor of the fuselage section was observed. Average floor-level accelerations were approximately 19.4-g's. In comparison, for an impact at only 31-fps an average floor-level acceleration of 29.9-g was obtained from a previous test of a similar fuselage section with a more conventional foam-filled subfloor [26]. Moreover, the foam filled subfloor used in the previous tests was 8% heavier than the deployable honeycomb energy absorbers.

6.2 Analytical Work

Due to the complex buckling and damage propagation modes, LS-DYNA was only able to capture the peak load for the three-point bend experiments. Future tests of this type will involve dynamic loading with the hope that some of the complex instabilities will be suppressed.

The level of correlation achieved by the LS-DYNA preliminary simulations of the fuselage section vertical drop test was quite good during the initial part of the honeycomb crush response. However, after 0.03 seconds, some significant differences were observed which can be attributed to the fact that the energy absorber was represented using solid elements instead of shells. The model relied on the input stress versus strain properties to mimic the response of the energy absorbers. While this approach worked well initially, the solid element model could not quite predict the complex failure mechanisms observed in the test article. As a follow-on research project,

the fuselage section model will be modified to include a shell element representation of the composite honeycomb energy absorbers.

7. Conclusions

The externally deployable composite honeycomb structure was demonstrated to be an effective energy absorber that could be utilized to manage the crash energy of light aircraft. During a 38.4 fps vertical drop test of a composite fuselage section, four energy absorbers crushed stably to about 70% of their 85% stroke capability. The small amount of rebound indicated that the energy absorbers dissipated nearly all of the kinetic energy in the fuselage section. The same was also true for an oblique impact test of the same fuselage section.

Acknowledgements

The authors would like to thank Dr. Ed Fasanella of NASA Langley for the discussions and comments concerning the LS-DYNA computer simulations. The technical support of Nelson Seabolt, David White, Donald Kepley, and Donald Smith is also acknowledged.

References

- [1] Shane J. S., "Design and Testing of an Energy-Absorbing Crewseat for the F/FB-111 Aircraft," NASA-CR-3916, August 1985.
- [2] Yosef V., BenMoshe A., Noyman Y., Gansman B., and Bradney C., "Rotorcraft External Airbag Protection System," AHS 62nd Annual Forum, Phoenix AZ, May 2006.
- [3] Wayne D. E., Cole J. K. and Rivellini T. P., "Mars Pathfinder Airbag Impact Attenuation System," AIAA-95-1552-CP, 13th AIAA Aerodynamic Decelerator Systems Technology Conference, Clearwater Beach Florida, May 1995.
- [4] Stein J. and Charles S., "Recent Developments in Inflatable Airbag Impact Attenuation Systems for Mars Exploration," 44th AIAA/ASME/ASCE/AHS SDM Conference, Norfolk Virginia, April 2003.
- [5] Cooper M., Sinclair R., Sanders J., and Frigerio J., "Design and Testing of an Airbag Landing Attenuator System for a Generic Crew Return Vehicle," Proceedings 18th AIAA Aerodynamic Decelerator Systems Technology Conference and Seminar, AIAA 2005-1616, 2005.
- [6] Smith R. H., "The Design and Development of Radio-Frequency Transparent Omnidirectional Energy-Absorbing Element Systems," NASA CR-66301, NVR-5114, January 1967.
- [7] Bixby H. W., "Development of a Paperboard Honeycomb Decelerator for Use With Large Platforms in Aerial Delivery Systems," USAF Report WADC-TR-59-776, 1959.

- [8] Schafer J. P., "Volumetrically Expandable Energy Absorbing Material," US Patent #3,339,673, September 1967.
- [9] Mehaffie S. R., "Foam Impact Attenuation System," AIAA 79-0416, AIAA 6th Aerodynamic Decelerator and Balloon Technology Conference, Houston, Texas, March 1979.
- [10] Kellas S., "Design, fabrication and testing of a crushable energy absorber for a passive Earth entry vehicle", NASA-CR-211425, 2002.
- [11] Kellas S., "An experimental investigation into the energy absorption performance of composite beam web for aircraft subfloor applications," National Technical Specialists' Meeting on Rotorcraft Structures, "Design Challenges and Innovative Solutions," Sponsored by the AHS, Oct. 1995.
- [12] Kellas S. and Knight N. F. Jr., "Design, Fabrication and Testing of Composite Energy-Absorbing Keel Beams for General Aviation Type Aircraft," AIAA-2001-1529, 42nd AIAA Structures, Structural Dynamics, and Materials Conference and Exhibit, Seattle, WA, April 16-19, 2001.
- [13] Wierzbicki T. and Bhat S., "A note on Shear Effects in Progressive Crushing of Prismatic Tubes," Society of Automotive Engineers, Paper #860821, 1987
- [14] Hayduk R. J. and Wierzbicki T., "Extensional collapse modes of structural members," NASA Conference Pub. 2245, *Research in Structural and Solid Mechanics*, 1982.
- [15] Wierzbicki T., "Crushing Analysis of Metal Honeycombs," *Int. J. Impact Engineering*, Vol.1, No.2, pp.157-174, 1983.
- [16] Wierzbicki T. and Abramowicz W., "On The Crushing Mechanics of Thin-Walled Structures," *J. of Applied Mechanics*, Vol. 50, pp.727-734, 1983.
- [17] Abramowicz W. and Jones N., "Dynamic Progressive Buckling of Circular and Square Tubes," *Int. J. Impact Engineering* Vol. 4, No. 4, pp. 243-270, 1986.
- [18] Abramowicz W. and Wierzbicki T., "Axial Crushing of Multicorner Sheet Metal Columns," *J. Applied Mechanics*, Vol. 56, pp.113-120, 1989.
- [19] Anon, "LS-DYNA Keyword User's Manual," Version 971, Livermore Software Technology Company, Livermore, CA, August 2006.
- [20] Matzenmiller, A., Lubliner, I. J., and Taylor, R. L., "A Constitutive Model for Anisotropic Damage in Fiber-Composites," *Journal of Mechanics and Materials*, Vol. 20, pp. 125-152, 1995.
- [21] Kellas, S. and Morton, J., "Scaling Effects in Angle-Ply Laminates," NASA Contractor Report 4423, February 1992.
- [22] Jackson, K. E., "Analytical Crash Simulation of Three Composite Fuselage Concepts and Experimental Correlation," *Journal of the American Helicopter Society*, Vol. 42, No. 2, April 1997, pp. 116-125.
- [23] Jackson, K. E., and Fasanella, E. L., "Innovative Composite Fuselage Design for Improved Crashworthiness," Proceedings of the 54th American Helicopter Society Forum and Technology Display, Washington DC, May 20-22, 1998.
- [24] Fasanella, E. L., and Jackson, K. E., "Analytical and Experimental Evaluation of Composite Energy Absorbing Subfloor Concepts," Proceedings of the AHS National Technical Specialists' Meeting on Rotorcraft Crashworthiness, September 14-17, 1998, Phoenix, AZ.
- [25] Jackson, K. E., "Impact Testing and Simulation of a Crashworthy Composite Fuselage Concept," *International Journal of Crashworthiness*, 2001, Vol. 6, No 1, pp.107-121.
- [26] Lyle, K. H.; Bark, L. W.; and Jackson, K. E., "Evaluation of Test/Analysis Correlation Methods for Crash Applications," *Journal of the American Helicopter Society*, Vol. 47, No. 4, October 2002, pp. 219-232.
- [27] Sareen, A. K., Sparks, C., Mullins, B. R., Fasanella, E. L., and Jackson, K. E., "Comparison of Soft Soil and Hard Surface Impact Performance of a Crashworthy Composite Fuselage Concept," Proceedings of the AHS Forum 58, Montreal, Canada, June 11-13, 2002.
- [28] Jackson, K. E., Fasanella, E. L., and Lyle, K. H., "Comparisons of the Impact Responses of a 1/5-Scale Model and a Full-Scale Crashworthy Composite Fuselage Section," Proceedings of the 59th American Helicopter Society Forum, Phoenix, AZ, 6-8 May 2003.
- [29] Fasanella, E. L., and Jackson, K. E., "Impact Testing and Simulation of a Crashworthy Composite Fuselage Section with Energy Absorbing Seats and Dummies," *Journal of the American Helicopter Society*, Vol. 49, No. 2, April 2004, pp. 140-148.
- [30] Fasanella, E. L., Jackson, K. E., Lyle, K. H., Sparks, C. E., and Sareen, A., "Multi-Terrain Impact Testing and Simulation of a Composite Energy Absorbing Fuselage Section," Proceedings of the American Helicopter Society Forum 60, Baltimore, MD, June 8-10, 2004.
- [31] Fasanella, Edwin L., Jackson, Karen E., Sparks, Chad E., and Sareen, Ashish K., "Water Impact Test and Simulation of a Composite Energy Absorbing Fuselage Section," *Journal of the American Helicopter Society*, Vol. 50, No. 2, April 2005, pp. 150-164.
- [32] Society of Automotive Engineers, Recommended Practice: Instrumentation for Impact Test - Part 1, Electronic Instrumentation, SAE J211/1, March 1995.